Design of High Torque Density Multi-Core Concentrated Flux-Type Synchronous Motors Considering Vibration Characteristics

Min-Ro Park, Jae-Woo Jung, Doo-Young Kim, Jung-Pyo Hong, *Senior Member, IEEE*, and Myung-Seop Lim

***Abstract*—This paper proposes a novel structure for the concentrated flux-type synchronous motor (CFSM) in order to improve the torque density, as well as the vibration characteristics. First, the conventional surface-mounted permanent magnet synchronous motor as prototype for the electric booster in the brake system is investigated through tests. Then, the relationship between the vibration characteristics and the number of poles and slots is analyzed. Based on the analysis results, a pole–slot combination for an improved CFSM is determined to enhance the vibration characteristics. Furthermore, a novel structure for the improved motor that employs three different core shapes in the rotor is proposed to increase the torque density. As a result, the improved motor with excellent vibration characteristics as well as a high torque density is designed. Finally, experiments are conducted to verify the effectiveness and the feasibility of the proposed method.**

***Index Terms*—Concentrated flux-type synchronous motor (CFSM), torque density, vibration.**

I. Introduction

TRACTION motors for X-electric vehicle (X-EV) are frequently operated as a generating mode during city driving. This regenerating operation of the traction motor helps to extend the total operating distance of the vehicle for one charge. In this operating mode, the vehicle needs additional braking force from the brake system. This is because the regenerative braking force is not enough to stop the vehicle due to the torque–speed characteristic of the traction motor. Moreover, the regenerative braking force of the traction motor varies with the speed of the vehicle. Therefore, in order to transmit more regenerative energy to the battery, the braking force generated by the brake system needs to be controlled actively as a change in the vehicle speed. However, the vacuum booster of the conventional brake system is not controlled as a change in the vehicle speed. To resolve this problem, an actively controllable booster, called an electric booster (E-booster), is required in the X-EV brake system. The operating mechanism of the brake system using the E-booster is described in the following and shown in Fig. 1. First, the electric control unit drives the electric motor according to the driver's braking requirements. Second, the electric motor produces the torque and the ball screw, which is placed inside of the hollow type motor, pushes the piston. The piston connected with the ball screw is then moved toward the master cylinder. The hydraulic pressure is generated in the master cylinder and operates the calipers. Finally, the braking force is produced. The brake system using the E-booster mainly consists of a hydraulic unit, electric control unit, master cylinder, ball screw, and electric motor [1]. Since these components are integrated, the brake

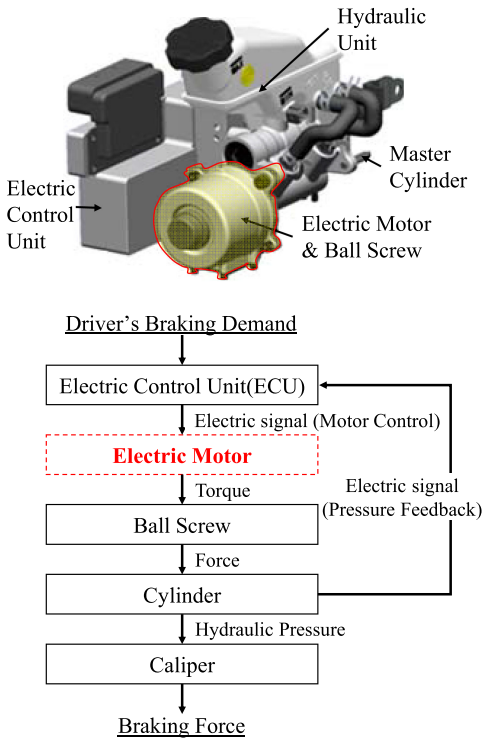

Fig. 1. Mechanism of the brake system using the E-booster.

Manuscript received June 19, 2018; revised September 22, 2018; accepted September 26, 2018. Date of publication October 15, 2018; date of current version February 20, 2019. Paper 2018-EMC-0476.R1, presented at the 2017 IEEE International Electric Machines and Drives Conference, Miami, FL, USA, May 21–24, and approved for publication in the IEEE TRANSACTIONS ON INDUSTRY APPLICATIONS by the Electric Machines Committee of the IEEE Industry Applications Society. (Min-Ro Park and Jae-Woo Jung contributed equally to this work). *(Corresponding author: Myung-Seop Lim.)*

M.-R. Park and J.-P. Hong are with the Department of Automotive Engineering, Hanyang University, Seoul 04763, South Korea (e-mail: minro1226@hanyang.ac.kr; hongjp@hanyang.ac.kr).

J.-W. Jung and D.-Y. Kim are with the Hyundai Mobis, Yongin-si 446-912, South Korea (e-mail: jjwoo@mobis.co.kr; dy9804@mobis.co.kr).

M.-S. Lim is with the School of Mechanical Engineering, Yeungnam University, Gyeongbuk 38541, South Korea (e-mail: limmang87@yu.ac.kr).

Color versions of one or more of the figures in this paper are available online at http://ieeexplore.ieee.org.

Digital Object Identifier 10.1109/TIA.2018.2876329

0093-9994 © 2018 IEEE. Personal use is permitted, but republication/redistribution requires IEEE permission.
See http://www.ieee.org/publications_standards/publications/rights/index.html for more information.

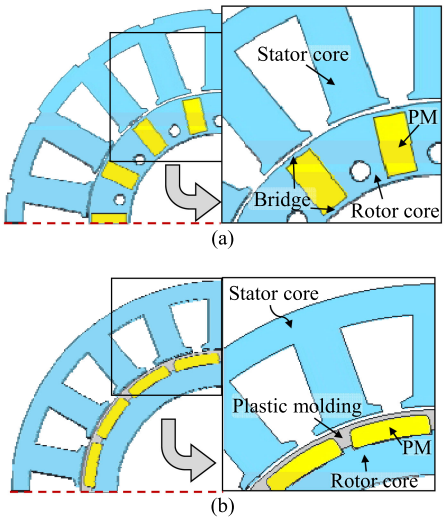

Fig. 2. Structure of the conventional CFSM and the SPMSM. (a) Conventional CFSM. (b) SPMSM.

system with the E-booster is a more compact system compared to a conventional brake system. The prototype of the surface-mounted permanent magnet synchronous motor (SPMSM) was designed to have a large hollow in the rotor structure so as to install the ball screw into the hollow. However, in this paper, the concentrated flux-type synchronous motor (CFSM) is adopted as an alternative to the prototype for the E-booster of the brake system in order to improve the torque density. Though there has been significant amount of research in the past on the CFSM [2]–[6], the size of the motors presented in this paper is larger and the inner diameter of the rotor cores is smaller compared to those of the motors used for the E-booster. Thus, there is a need to study on the small-sized CFSM for the E-booster. Also, this large hollow limits the amount of permanent magnet (PM) to be inserted in the rotor core and the small amount of PM results in a low torque density. The torque density can be improved by narrowing the bridge and reducing the leakage flux. On the other hand, since the bridge is important for preventing PMs from scattering as shown in Fig. 2(a), the shape of the bridge has to be determined by considering the structural safety. However, an increase in torque density generally leads to an increase in vibration. Therefore, when designing the high torque density of the CFSM, the vibration characteristics should also be taken into consideration. The authors in [7] and [8] examined the vibration characteristics as well as the torque characteristics of the CFSM. However, these studies lack theoretical approaches and focus only on the comparison of simulation results according to the number of poles and slots.

In this paper, in order to improve the motor characteristics in consideration of the above-mentioned constraints, a new structure of CFSM is proposed. First, the prototype of the SPMSM is analyzed through simulation and test. This analysis determines the goals of the improvement design and the relationship between the design parameters and the motor performance is derived. Based on these analyses, the improvement design is carried out considering the vibration characteristics. Through the mathematical relationship between the number of poles and slots and the electromagnetic force that causes the vibrations, the number of poles and slots in the improved model is determined. In addition, to improve the torque density, three shapes of rotor cores are proposed depending on the presence or absence of bridges. Core shape 1 has bridges on both the air-gap side and the shaft side. Core shape 2 only has a bridge on the shaft side. Core shape 3 does not have any bridge so as to maximize the torque density. As the number of bridges is minimized, the leakage flux can be reduced and the torque density can be improved. Finally, the proposed structure and design methodology are verified by testing the fabricated improvement model.

II. Analysis of Prototype

A. Limit of the Prototype

The prototype of the SPMSM for the E-booster is shown in Fig. 2(b). The SPMSM is suitable for the hollow-type motor because the PMs are mounted on the surface of the rotor core, making the rotor structure simple. However, the SPMSM designed for automotive application usually needs retainers to keep PMs from scattering and this additional structure increases the magnetic air-gap length. As a result, the increase in the air-gap length leads to the low torque density. To improve this weakness, the CFSM is a good alternative for its similar level of output power because it has a shorter magnetic air-gap length and uses a large amount of PM.

However, the improvement in the torque density of the electric motor causes an increase in vibrations due to the electromagnetic force. Equation (1) shows the Maxwell stress tensor method. As shown in (1), the high magnetic flux density in the air gap not only improves the torque density but also increases the radial electromagnetic force applied to the stator core. The increased radial electromagnetic force deteriorates the vibration characteristic as shown in the following:

$$f_r = \frac{B_{g_r}^2 - B_{g_t}^2}{2\mu_0}, \quad f_t = \frac{B_{g_r} \cdot B_{g_t}}{\mu_0} \tag{1}$$

where f_r and f_t are the radial and tangential electromagnetic force densities, respectively, μ_0 is the vacuum permeability. B_{g_r} and B_{g_t} are the radial and tangential components of the air-gap magnetic flux density, respectively.

Therefore, there is a need for a design methodology that increases the torque density, and thus improves the vibration characteristics of the electric motor. To analyze the vibration characteristics of the prototype, a vibration test was conducted. Fig. 3 shows the results of the prototype vibration test. The test was performed at 2000 r/m, 1.5 N·m. The fundamental component of the line frequency f of the prototype is 266.67 Hz because it has 16 poles. As shown in the test results, the magnitude of the maximum vibration was 0.23 g at 1 g = 9.81 m/s^2, and the frequency of the maximum vibration occurred at 533.34 Hz, which is two times the line frequency $2f$.

B. Calculation of Radial Electromagnetic Force Using Finite Element Analysis (FEA)

In order to identify the cause of the maximum vibration of the prototype, the radial electromagnetic force was calculated by using the FEA in the load condition of 2000 r/m, 1.5 N·m. The

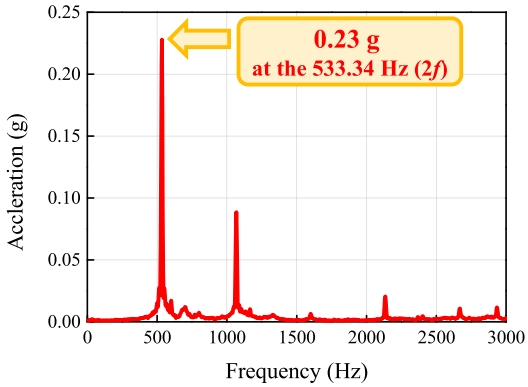

Fig. 3. Vibration test result of the prototype.

calculated radial electromagnetic force was separated by time and spatial harmonic order through a spectrum analysis. The spatial harmonics are the spatial distributions based on 360° of mechanical angle and the spatial harmonic order is called the vibration order r and the time harmonic order is a multiple of the line frequency f. Furthermore, the relationship between displacement d and vibration order r is as follows:

$$d \propto \frac{1}{r^4}. \tag{2}$$

By taking into consideration the circumferential vibration modes of the stator core, the displacement of the stator core is an inverse function of the fourth power of the vibration order [9]. In other words, the minimum vibration order has a significant impact on the vibration. Therefore, the value obtained by dividing the radial electromagnetic force by r^4 is defined as the effective force.

Fig. 4(a) shows a spectrum analysis of the radial electromagnetic force calculated by FEA. As seen in the test results, the magnitude of the radial electromagnetic force is the largest at 2f. Moreover, Fig. 4(b) and (c) shows the radial electromagnetic force and effective force according to the vibration order at 2f. As shown in Fig. 4(b) and (c), the main vibration source in the 2f is the minimum vibration order $r = 2$. Thus, in the next section, the radial electromagnetic force is analyzed using analytic method to determine the design direction.

C. Analysis of the Radial Electromagnetic Force Using an Analytic Method

In case of PMSM, the magnetic field distribution of the air gap is determined by the PM field, the armature reaction field and the slot effect represented by the relative permeance. When the magnetic saturation is ignored, the radial component of the magnetic flux density in the air gap can be expressed as follows:

$$B_{g_r} = (B_{r_\mathrm{mag}} + B_{r_\mathrm{arm}})\Lambda_a \tag{3}$$

where B_{r_mag} and B_{r_arm} are the slotless magnetic flux density in the air gap by the PM and that by the armature reaction, respectively. Λ_a is a relative specific permeance, which is a component separated from the constant term λ_0 in the relative permeance λ_a in (6).

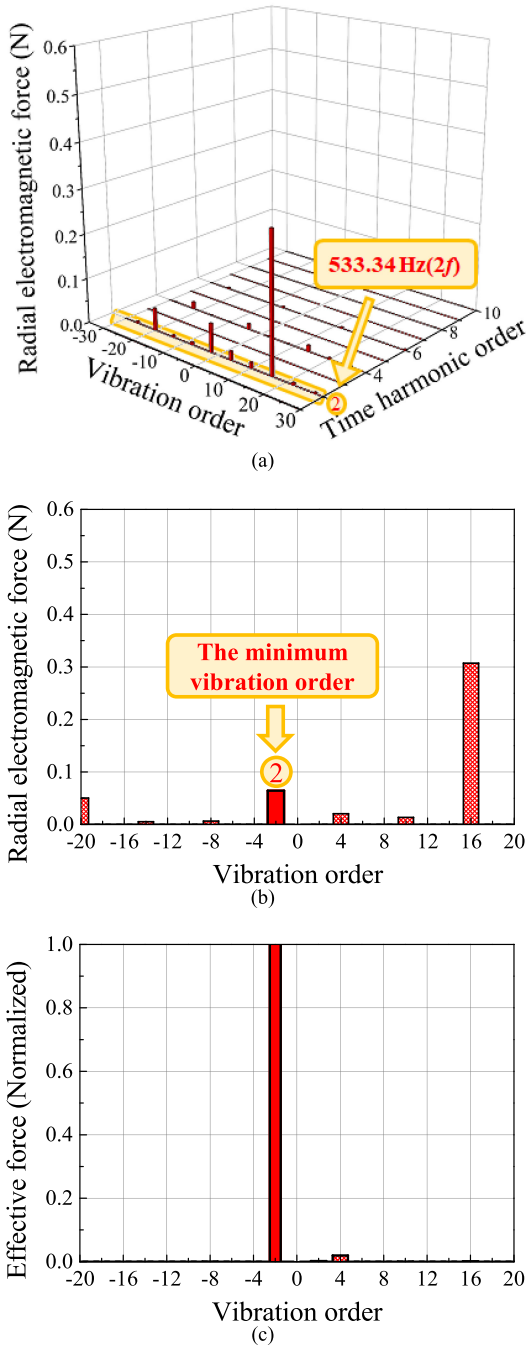

Fig. 4. Radial electromagnetic force and effective force of the prototype. (a) Radial electromagnetic force spectrum. (b) Radial electromagnetic force at the 2f. (c) Effective force at the 2f.

The three terms on the air-gap magnetic flux density can be represented in the form of Fourier series, as follows:

$$B_{r_\mathrm{mag}} = \sum_{\mu} B_{m\mu} \cos\left(\mu\omega t - \mu p\theta + \phi_\mu\right) \tag{4}$$

$$B_{r_\mathrm{arm}} = \sum_{n}\sum_{\nu} B_{an\nu} \cos\left(n\omega t - \nu p\theta + \phi_{n\nu}\right) \tag{5}$$

$$\lambda_a = \lambda_0\Lambda_a = \lambda_0\left[1 + \sum_{k} \Lambda_{ak} \cos\left(ks\theta\right)\right] \tag{6}$$

where p is the pole pairs, s is the number of stator slots, θ is the mechanical angle, t is the time, ω is $2\pi f$, f is the fundamental component of the line frequency, n is the time harmonic order of the current, μ is the spatial harmonic order of the air-gap magnetic flux density by PM and the positive integer, and ν is the spatial harmonic order of the air-gap magnetic flux density by the armature reaction and is determined by the winding. The winding is also set by the combination of poles and slots. ν can be obtained using (7)–(9) [10]

$$q = \frac{s}{2pm} = \frac{z}{a} \tag{7}$$

where m is the number of phases, z is the numerator of q, a is the denominator of q. z and a are relatively prime.

If a is odd, then ν is

$$\nu = \pm\frac{1}{a}(2mk+1). \tag{8}$$

If a is even, then ν is

$$\nu = \pm\frac{1}{a}(2mk+2) \tag{9}$$

where k is an integer. The $\pm$ sign in (8) and (9) is chosen to be $+$ or – to make the equations yield the positive sign for the fundamental ($\nu = +1$).

Neglecting the tangential component of magnetic flux density in the air gap [11], the following radial electromagnetic force density can be calculated by Maxwell's stress tensor method:

$$f_r = \frac{B_{g_r}^2 - B_{g_t}^2}{2\mu_0} \approx \frac{B_{g_r}^2}{2\mu_0}. \tag{10}$$

The radial electromagnetic force density can be obtained by substituting (4)–(6) into (10). It is expressed as follows:

$$\begin{aligned} f_r &\approx \frac{B_{g_r}^2}{2\mu_0} \\ &= \frac{1}{2\mu_0}\left[\begin{array}{c}\sum\limits_{\mu} B_{m\mu}\cos(\mu\omega t - \mu p\alpha + \phi_\mu) \\ +\sum\limits_{n}\sum\limits_{\nu}\left[B_{an\nu}\cos(n\omega t - \nu p\alpha + \theta_{n\nu})\right]\end{array}\right]^2 \\ &\quad\times\left[1+\sum_{k}\Lambda_{ak}\cos(ks\alpha)\right]^2. \end{aligned} \tag{11}$$

From the above equation, the vibration order and frequency of the radial electromagnetic force can be summarized as shown in Table I. As shown in the table, the vibration order and frequency of the radial electromagnetic force are determined by the number of poles and slots. Given the interaction of the PM and armature reaction field equation in Table I, assuming that the armature current is sinusoidal ($n = 1$), when μ is 1, the magnetic force of $2f$ frequency component occurs. Therefore, ν should be $-5/4$ to generate the force with a vibration order of 2. In other words, the radial electromagnetic force of the vibration order $r = 2$ is generated by the interaction between the $\mu = 1$ component of the magnetic flux density by the PM and the $\nu = -5/4$ sub-harmonic component of the magnetic flux density by the armature reaction at the air gap. Among these two components, the magnetic flux density by the PM contributes to the output power. However, the sub-harmonic component of the magnetic flux density by the armature reaction is independent from the output power. Therefore, by reducing the sub-harmonic of the air-gap magnetic flux density by the armature reaction, a design that reduces the radial electromagnetic force of the vibration order $r = 2$ is needed. Section III provides an improved design that reduces vibration and improves torque density through the previous analysis.

TABLE I
VIBRATION ORDER AND FREQUENCY OF RADIAL ELECTROMAGNETIC FORCE

Source	Vibration order	Frequency
Permanent magnet fields	$p(\mu_1 \pm \mu_2)$	$(\mu_1 \pm \mu_2)f$
Armature reaction fields	$p(\nu_1 \pm \nu_2)$	$(n_1 \pm n_2)f$
Interaction of the permanent magnet and armature reaction fields	$p(\mu \pm \nu)$	$(\mu \pm n)f$
Interaction of the permanent magnet field and stator slotting	$(\mu_1 \pm \mu_2)p \pm ks$ or $(\mu_1 \pm \mu_2)p \pm (k_1 \pm k_2)s$	$(\mu_1 \pm \mu_2)f$
Interaction of the armature reaction field and stator slotting	$(\nu_1 \pm \nu_2)p \pm ks$ or $(\nu_1 \pm \nu_2)p \pm (k_1 \pm k_2)s$	$(n_1 \pm n_2)f$

III. IMPROVED DESIGN

A. Design Objectives

The limitations and goals mentioned earlier are summarized as follows:

1) large hollow type rotor;
2) small motor;
3) reduction of vibrations;
4) improvement of torque density.

The improved CFSM is designed to overcome the aforementioned design limitations and improve the mechanical and electrical performance compared to the prototype. In addition, when designing the higher torque density, the vibration characteristics should be considered in the design process. In particular, in order to reduce the vibration of $2f$, the radial electromagnetic force of the prototype was analyzed in Section II using an FEA and an analytical approach. Based on this analysis, the number of poles and slots was determined as design parameters in order to improve the vibration characteristics. Next, so as to increase the torque density, a new structure for reducing the leakage magnetic flux is proposed. The new structure is made by laminating the cores with different shape in the axial direction.

TABLE II
COMPARISON OF CHARACTERISTICS ACCORDING TO THE NUMBER OF POLES AND SLOTS

Pole / Slot	Winding factor		LCM	Vibration order
	Fundamental	Sub-harmonic		
12 / 18	0.866	-	36	6
14 / 18	0.902	-0.750 (-5/7th)	126	2
16 / 18	0.945	-0.923 (-5/4th)	144	2

B. Determination of Pole–Slot Combination Considering Vibration Characteristics

As previously discussed, the vibration characteristics as well as the torque density should be considered. The number of poles and slots is an important parameter that determines the performance of the motor. First, the input frequency of the inverter must be increased in proportion to the number of poles [12], [13]. In other words, the increase in the number of poles has to increase the inverter input frequency, and the rising input frequency is burdensome to the inverter. Therefore, in this paper, the number of poles is limited to less than 16 poles in order to minimize the burden of the inverter. Also, the number of stator slots is considered to be equal to the number of slots of the prototype. Second, the torque can be estimated by the winding factor [14]. Because the winding factor of the fundamental is related to the effective turns of the coil, which are directly proportional to the torque, the winding factor can be considered to increase the torque density. Third, the least common multiple (LCM) of the number of poles and slots significantly affects the magnitude of the cogging torque. As the LCM increases, the cogging torque decreases [15]. Finally, as analyzed in Section II, the number of poles and slots determines the spatial harmonic order including sub-harmonic of the air-gap magnetic flux density by the armature reaction and the frequency and vibration order of the electromagnetic forces that cause the motor to vibrate. Table II shows the winding factor of the fundamental component and sub-harmonic component generating the minimum vibration order, LCM of the number of poles and slots, and the minimum vibration order of the $2f$ according to the numbers of poles and slots. The vibration characteristics of the combination of 12 poles and 18 slots are expected to be the best because of its high vibration order. On the other hand, its torque density is predicted to be the smallest because of its smallest winding factor. Moreover, its LCM is much smaller which results in a large magnitude of cogging torque. The combination of the 14 poles and 18 slots and a combination of the 16 poles and 18 slots have a high winding factors and LCM. However, the vibration order is 2. The vibration order 2 of the combination of 16 poles and 18 slots, which is the combination of the poles and slots of the prototype, is generated by the $-5/4$ sub-harmonic, and the vibration order 2 of the combination of 14 poles and 18 slots is generated by the $-5/7$ sub-harmonic. Comparing the winding factors of the sub-harmonic generating vibration order 2, it can be expected that the vibration characteristics of the 14 pole and 18 slot will perform better.

Therefore, in this study, the number of poles and slots of the improved model was determined to be 14 poles and 18 slots in order to improve the vibration characteristics of the prototype considering the torque density.

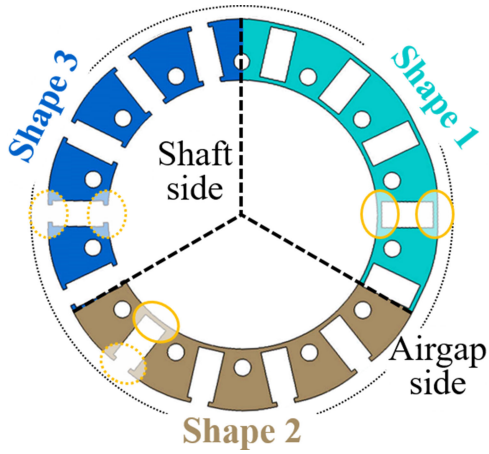

Fig. 5. Core shapes of the multi-core CFSM.

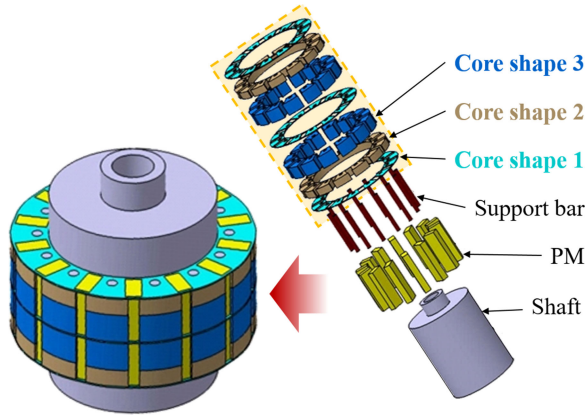

Fig. 6. Rotor structure of the multi-core CFSM.

C. Structure of Improved CFSM

In this paper, a novel structure for the CFSM rotor is proposed to improve the torque density in a limited space such as a large hollow-type rotor and a small-sized motor. The best way to increase the torque density is to remove the leakage flux path in the bridge of the rotor core. However, the bridges cannot be eliminated for structural stability. Therefore, three different core shapes can be classified according to the presence or absence of the bridges. As shown in Fig. 5, first, the cores of shape 1 have bridges on both the air-gap side and the shaft side. Second, the cores of shape 2 have a bridge only on the shaft side. Finally, the cores of shape 3 do not have any bridge so as to maximize the torque density. All bridges on the shaft side are installed for insertion of the shaft and maintaining the shape of the rotor core against the stress by the centrifugal force. Also, the bridges of the air-gap side protect PMs from scattering by the centrifugal force. These three core shapes are laminated to form a rotor. As a result, the structure of the rotor is composed of three different core shapes as shown in Fig. 6. The cores of shape 1 are positioned at the top, bottom, and center of the rotor core assembly for structural stability. The motor with this structure is

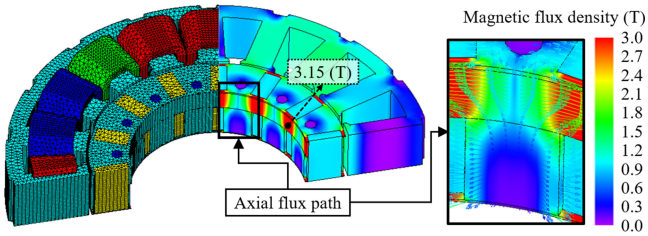

Fig. 7. Three-dimensional FEA model and magnetic flux density distribution under the no-load condition.

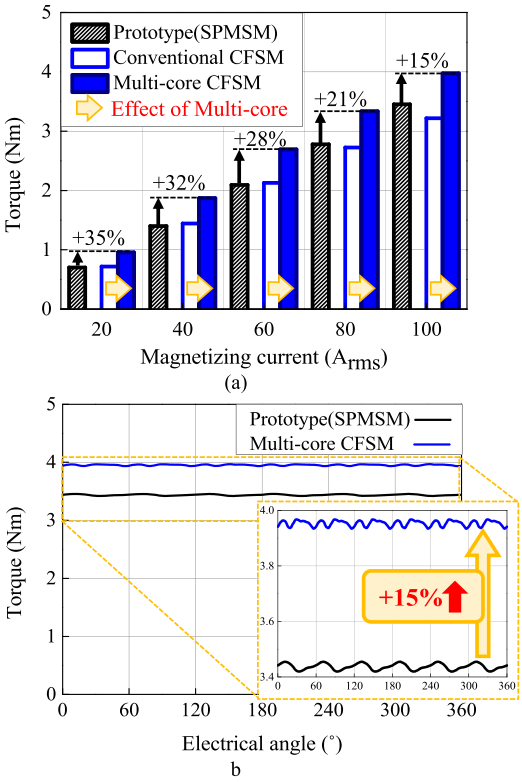

Fig. 8. Torque characteristics. (a) Torque according to the magnetizing current of each model. (b) Torque waveform at $100A_{\text{rms}}$.

called a multi-core motor in this paper. Furthermore, the material for the shaft and support bar is non-magnetic steel, SUS304 for minimization of leakage flux.

The multi-core CFSM has axial flux paths due to three different shapes of rotor cores as shown in Fig. 7. Therefore, a three-dimensional FEA is required for precise calculation. To confirm the effect of the multi-core, the torques of the prototype, conventional CFSM and multi-core CFSM of same size are compared according to the armature current. The simulation results are shown in Fig. 8(a). First, the effect of multi-core can be confirmed by comparing the torque of conventional CFSM and multi-core CFSM. The torque of multi-core CFSM increased by 20%–30% according to load condition as compared with the torque of conventional CFSM. Furthermore, even when compared with the prototype torque, the torque of the multi-core was increased. In particular, as shown in Fig. 8(b), the maximum torque increased by 15% and the torque ripple decreased from 1.0% to 0.8%. Furthermore, Fig. 9 shows the current waveforms of the prototype and the improved model obtained by using the

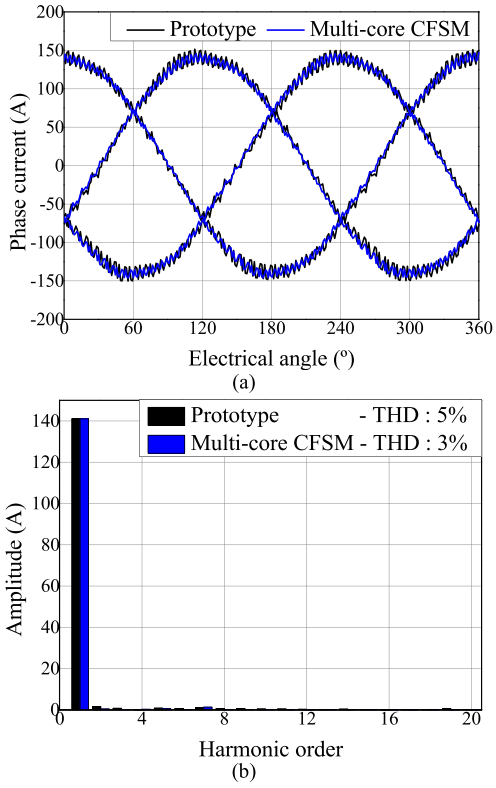

Fig. 9. Current characteristics. (a) Current waveform at $100A_{\text{rms}}$. (b) Harmonic analysis.

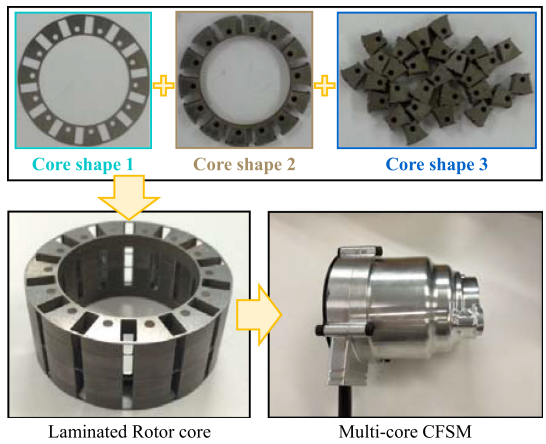

Fig. 10. Fabricated the multi-core CFSM.

simulation at maximum torque. The total harmonic distortion of the improved model's current is about 3%, which is about 2% lower than that of prototype's current.

Therefore, as shown in Fig. 10, the multi-core CFSM is fabricated by laminating the three shape cores. Then, the fabricated model is tested for verification in the following section.

IV. Design Result and Verification

A. Torque, Current, and Efficiency-Speed Characteristics

Performance, such as torque, speed, and armature current of the designed multi-core CFSM, is calculated by using the *d*- and *q*-axis equivalent circuit and the voltage equation considering the iron loss [16], [17]. The voltage equations and the output

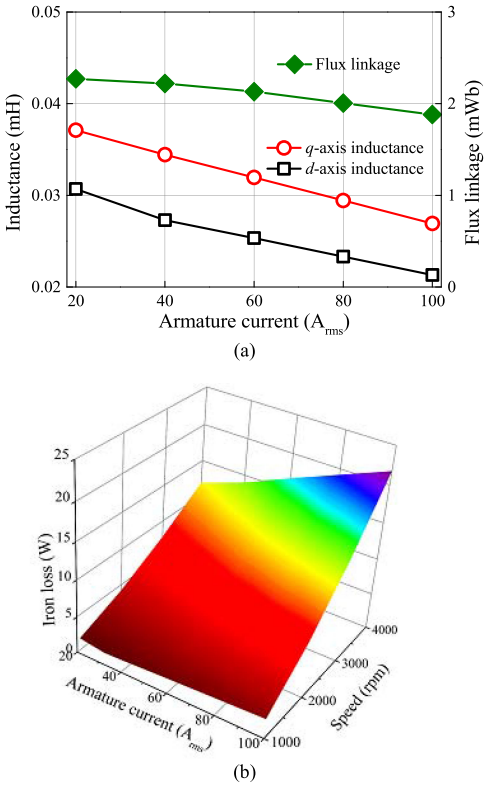

Fig. 11. Circuit parameter under load condition. (a) Flux linkage and inductance. (b) Iron loss.

torque are expressed as follows:

$$\begin{bmatrix} v_d \\ v_q \end{bmatrix} = R_a \begin{bmatrix} i_{od} \\ i_{oq} \end{bmatrix} + \left(1 + \frac{R_a}{R_c}\right) \begin{bmatrix} v_{od} \\ v_{oq} \end{bmatrix} + p \begin{bmatrix} L_d & 0 \\ 0 & L_q \end{bmatrix} \begin{bmatrix} i_{od} \\ i_{oq} \end{bmatrix} \tag{12}$$

$$\begin{bmatrix} v_{od} \\ v_{oq} \end{bmatrix} = \begin{bmatrix} 0 & -\omega L_q \\ \omega L_d & 0 \end{bmatrix} \begin{bmatrix} i_{od} \\ i_{oq} \end{bmatrix} + \begin{bmatrix} 0 \\ \sqrt{3}\omega\psi_e \end{bmatrix} \tag{13}$$

$$T = P_n \left[\sqrt{3}\psi_e i_{oq} + (L_d - L_q)\, i_{od} i_{oq}\right]. \tag{14}$$

Subscripts d and q refer to the d- and q-axis components; i and v are the armature current and voltage, respectively; R_a is the phase resistance; R_c is the equivalent resistance of the iron loss; L is inductance; ψ_e is the flux linkage of the PM in rms; and ω is the electrical speed in rad/s.

In order to calculate the performance using the equivalent circuit, the flux linkage, the inductance, and the iron loss are obtained via a nonlinear FEM. The phase angle of the armature current was fixed at 0° because the designed multi-core CFSM is driven by $i_d = 0°$ control. The flux linkage and the d-, q-axis inductance according to the armature currents of 20–100 A_{rms} are shown in Fig. 11(a). As the armature current increases, the saturation effect of the core causes a decrease in d-axis and q-axis inductances. Fig. 11(b) shows the iron loss map according to the armature currents of 20–100 A_{rms} and speeds of 1000–4000 r/m. The performance was evaluated using a d–q-axis equivalent circuit and estimated parameters. Then, the load test of the model was performed to verify the simulation results. The

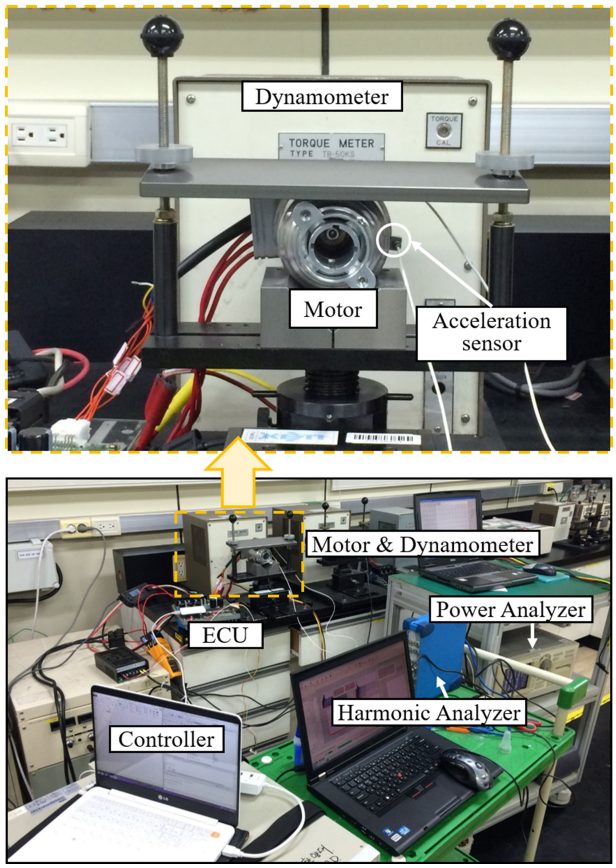

Fig. 12. Experimental setup for load and vibration test.

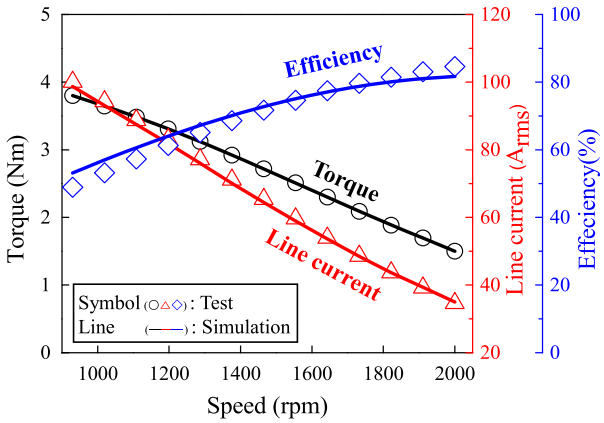

Fig. 13. Comparison of the torque, current, and efficiency of improved model according to the speed: Simulation versus test.

experimental setup for load test is shown in Fig. 12. The motor was driven by $i_d = 0°$ control.

Fig. 13 shows the simulation and test results of the torque, line current, and efficiency according to the speed. When comparing the line current input to the motor at the same torque, the maximum error is less than 2%. In addition, the difference in efficiency is smaller than 5%, which is acceptable.

B. Vibration Characteristics

The radial electromagnetic force of the improved model was also calculated using FEA. Fig. 14(a) shows the spectrum

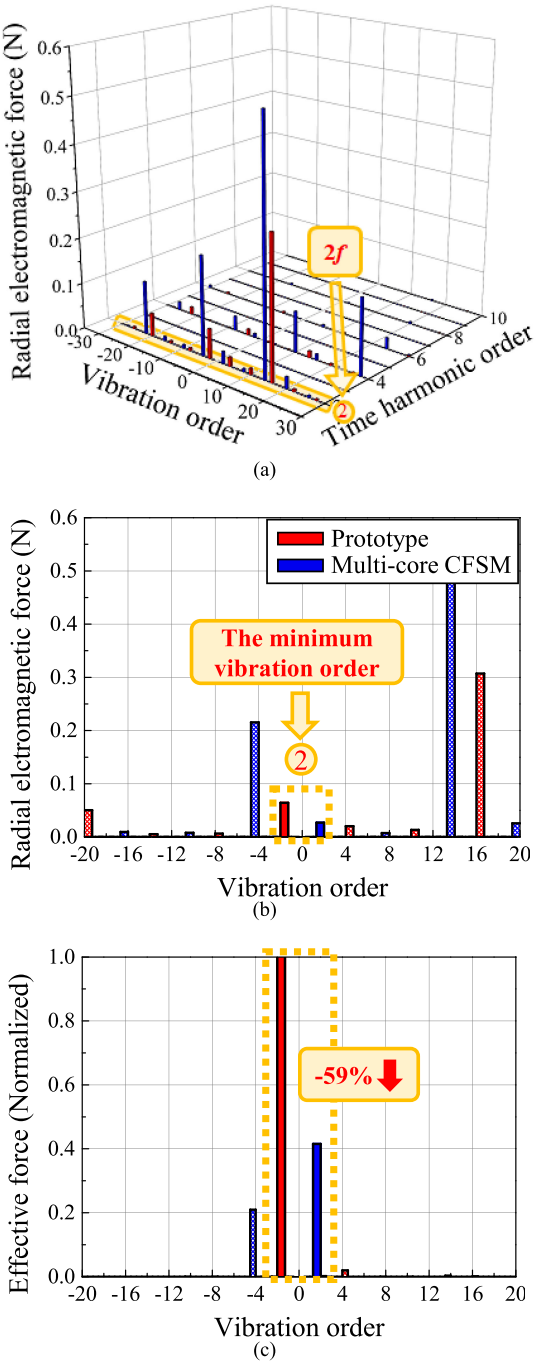

Fig. 14. Radial electromagnetic force and effective force of the prototype and improved model. (a) Radial electromagnetic force spectrum. (b) Radial electromagnetic force at the 2*f*. (c) Effective force at the 2*f*.

analysis of the radial electromagnetic force of the prototype and the improved model. The radial electromagnetic force in the 2*f* is larger than that at the other frequencies. Also, Fig. 14(b) and (c) shows the radial electromagnetic force and effective force according to the vibration order at 2*f*. The minimum vibration order of radial electromagnetic force of both models in the 2*f* is 2. However, the magnitude of the radial electromagnetic force of the minimum vibration order is different. Considering the magnitude of the radial electromagnetic force and effective force with the minimum vibration order of the prototype and

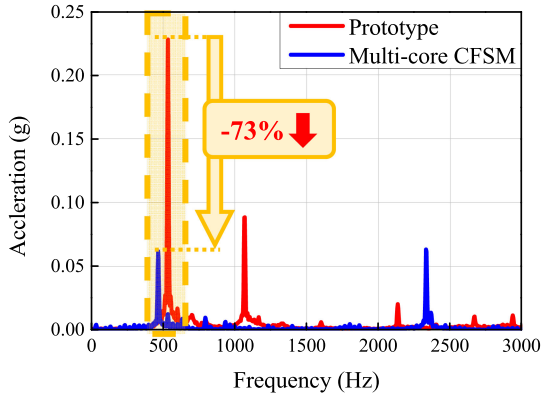

Fig. 15. Vibration test result of the prototype and improved model.

TABLE III
DESIGN RESULTS OF PROTOTYPE AND IMPROVED MODEL

Quantity	Prototype	Improved model (Multi-core CFSM)
DC link voltage (V_{dc})	12	
Current limit (A_{rms})	100	
Pole / Slot	16 / 18	14 / 18
Stator diameter (mm)	76	
Rotor diameter (mm)	50.9	46.6
Stack length (mm)	20.1	
Mechanical airgap length (mm)	0.4	
Torque density (kNm/m^3)	36.2	41.7 (+15%)

the improved model, the vibration characteristics in the 2*f* of the improved model are better than that of the prototype. This is because the magnitude of the radial electromagnetic force of vibration order 2 is smaller. In particular, the magnitude of the effective force considering the displacement of the stator was reduced by about 59%.

Next, the effect of reducing the effective force on the vibration is verified through experiment results. As seen in the experimental configuration in Fig. 11, the acceleration sensor is attached to the surface of the housing to measure the translational vibration of the motor. The load condition is 1.5 N·m at 2000 r/m. Fig. 15 shows the experiment results measured with an acceleration sensor. The vibration of the improved model at the 2*f* is 0.06 g. Compared with the vibration of the prototype, the vibration of the improved model was reduced by about 73% at the 2*f*.

In conclusion, the design results of the prototype and the improved model are summarized in Table III. The torque density of the improved model applied with the proposed structure is about 15% higher than that of the prototype at the same input conditions (voltage, current) and dimension (outer diameter, axial length). In addition, the pole–slot combination was changed to improve the vibration characteristics. All of these results were verified through testing.

V. CONCLUSION

This paper proposes a design method and novel structure of the CFSM to improve vibration characteristics and the torque

density. At first, the SPMSM as the prototype is investigated through the vibration test. Then, the relationship between the vibration characteristics and the pole–slot combination is analyzed. Based on the analysis results, the pole–slot combination for the improved CFSM is determined to enhance the vibration characteristics. Furthermore, the multi-core CFSM using three kinds of rotor core is proposed to minimize leakage flux and increase the torque density. As a result, the improved motor achieves better vibration characteristics and higher torque density than that of SPMSM. The torque density increased by about 15% and the effective force decreased by 59%. Finally, the experiment is conducted to verify the effectiveness and the feasibility of the proposed method and the structure in the paper.

REFERENCES

[1] J. Kim, S. Ko, G. Lee, H. Yeo, P. Kim, and H. Kim, "Development of co-operative control algorithm for parallel HEV with electric booster brake during regenerative braking," in *Proc. 2011 IEEE Vehicle Power Propulsion Conf.*, Chicago, IL, USA, 2011, pp. 1–5.

[2] S. I. Kim, S. Park, T. Park, J. Cho, W. Kim, and S. Lim, "Investigation and experimental verification of a novel spoke-type ferrite-magnet motor for electric-vehicle traction drive applications," *IEEE Trans. Ind. Elec.*, vol. 61, no. 10, pp. 5763–5770, Oct. 2014.

[3] S. I. Kim, J. Cho, S. Park, T. Park, and S. Lim, "Characteristics comparison of a conventional and modified spoke-type ferrite magnet motor for traction drives of low-speed electric vehicles," *IEEE Trans. Ind. Appl.*, vol. 49, no. 6, pp. 2516–2523, Nov./Dec. 2013.

[4] S. J. Galioto, P. B. Reddy, A. M. EL-Refaie, and J. P. Alexander, "Effect of magnet types on performance of high-speed spoke interior-permanent-magnet machines designed for traction applications," *IEEE Trans. Ind. Appl.*, vol. 51, no. 3, pp. 2148–2160, May/Jun. 2015.

[5] J. M. Kim, S. H. Chai, M. H. Yoon, and J. P. Hong, "Plastic injection molded rotor of concentrated flux-type ferrite magnet motor for dual-clutch transmission," *IEEE Trans. Magn.*, vol. 51, no. 11, pp. 1–4, Nov. 2015.

[6] H. J. Kim, D. Y. Kim, and J. P. Hong, "Structure of concentrated-flux-type interior permanent-magnet synchronous motors using ferrite permanent magnets," *IEEE Trans. Magn.*, vol. 50, no. 11, pp. 1–4, Nov. 2014.

[7] E. Carraro, N. Bianchi, S. Zhang, and M. Koch, "Design and performance comparison of fractional slot concentrated winding spoke type synchronous motors with different slot-pole combinations," *IEEE Trans. Ind. Appl.*, vol. 54, no. 3, pp. 2276–2284, May/Jun. 2018.

[8] M. R. Park, D. Y. Kim, J. W. Jung, and J. P. Hong, "Design of high torque density multi-core concentrated flux-type synchronous motors considering vibration characteristic," in *Proc. 2017 IEEE Int. Electric Machines Drives Conf.*, Miami, FL, USA, 2017, pp. 1–6.

[9] J. F. Cieras, C. Wang, and J. C. Lai, *Noise of Polyphase Electric Motors*. Boca Raton, FL, USA: Taylor & Francis/CRC Press, 2006.

[10] D. Y. Kim, M. R. Park, J. H. Sim, and J. P. Hong, "Advanced method of selecting number of poles and slots for low-frequency vibration reduction of traction motor for elevator," *IEEE/ASME Trans. Mechatronics*, vol. 22, no. 4, pp. 1554–1562, Aug. 2017.

[11] R. Islam and I. Husain, "Analytical model for predicting noise and vibration in permanent-magnet synchronous motors," *IEEE Trans. Ind. Appl.*, vol. 46, no. 6, pp. 2346–2354, Nov./Dec. 2010.

[12] M. S. Lim, S. H. Chai, J. S. Yang, and J. P Hong, "Design and verification of 150 krpm PMSM based on experiment result of prototype," *IEEE Trans. Ind. Elec.*, vol. 62, no. 12, pp. 7827–7836, Dec. 2015.

[13] H. J. Kim, J. S. Jeong, M. H. Yoon, J. W. Moon, and J. P. Hong, "Simple size determination of permanent-magnet synchronous machines," *IEEE Trans. Ind. Elec.*, vol. 64, no. 10, pp. 7972–7983, Oct. 2017.

[14] Y. Yoko, T. Higuchi, and Y. Miyamoto, "General formulation of winding factor for fractional-slot concentrated winding design," *IET Electr. Power Appl.*, vol. 10, no. 4, pp. 231–239, 2016.

[15] J. M. Kim, M. H. Yoon, J. P. Hong, and S. I. Kim, "Analysis of cogging torque caused by manufacturing tolerances of surface-mounted permanent magnet synchronous motor for electric power steering," *IET Electr. Power Appl.*, vol. 10, no. 8, pp. 691–696, Sep. 2016.

[16] B. H. Lee, S. O. Kwon, T. Sun, J. P. Hong, G. H. Lee, and J. Hur, "Modeling of core loss resistance for d-q equivalent circuit analysis of IPMSM considering harmonic linkage flux," *IEEE Trans. Magn.*, vol. 47, no. 5, pp. 1066–1069, May 2011.

[17] M. S. Lim, J. M. Kim, Y. S. Hwang, and J. P. Hong, "Design of an ultra-high-speed permanent-magnet motor for an electric turbocharger considering speed response characteristics," *IEEE/ASME Trans. Mechatronics*, vol. 22, no. 2, pp. 774–784, Apr. 2017.

Min-Ro Park received bachelor's degree in electrical engineering from Chungnam National University, Daejeon, South Korea, in 2013. He is currently working toward the Ph.D. degree in automotive engineering from Hanyang University, Seoul, South Korea.

His research interests include design and analysis of electric machine for electromechanical system.

Doo-Young Kim received bachelor's degree in mechanical engineering and the Ph.D. degree in automotive engineering from Hanyang University, South Korea, in 2012 and 2018, respectively.

He is currently a Research Engineer with Hyundai Mobis Co., Yongin, South Korea. His research interests include electric machine design for automotive applications, and analysis of vibration and noise of electric machine.

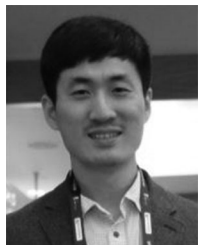

Jae-Woo Jung received the B.S. and M.S. degrees in electrical engineering from Changwon National University, Changwon, South Korea, in 2005 and 2007, respectively, and the Ph.D. degree in automotive engineering from Hanyang University, Seoul, South Korea, in 2013.

From 2009 to 2012, he had developed PMSM for automotive application. Since 2013, he has been a Research Staff Member with the R&D Center, Hyundai Mobis Co. Ltd., Yongin, South Korea. His research interests include the design and analysis of various electromagnetic devices for electromechanical brake system.

Jung-Pyo Hong (SM'97) received the Ph.D. degree in electrical engineering from Hanyang University, Seoul, South Korea, in 1995.

From 1996 to 2006, he was a Professor with Changwon National University, Changwon, South Korea. Since 2006, he has been working as a Professor with the Hanyang University, Seoul, South Korea. His research interests include the design of electric machines, optimization, and numerical analysis of electromechanics.

Myung-Seop Lim received the bachelor's degree in mechanical engineering and the master's and Ph.D. degrees in automotive engineering from Hanyang University, Seoul, South Korea, in 2012, 2014, and 2017, respectively.

From 2017 to 2018, he was a Research Engineer with Hyundai Mobis, Yongin, South Korea. Since 2018, he has been with Yeungnam University, Daegu, South Korea, where he is currently an Assistant Professor. His research interests include electromagnetic field analysis and electric machinery for mechatronics systems, such as automotive and robot applications.